International Journal of Heat and Mass Transfer 80 (2015) 748–758

Contents lists available at ScienceDirect

International Journal of Heat and Mass Transfer

journal homepage: www.elsevier.com/locate/ijhmt

Turbulent convective heat transfer of CO_2 in a helical tube at near-critical pressure

Jinliang Xu [a,*], Chuanyong Yang [b], Wei Zhang [a], Dongliang Sun [a,*]

[a] The Beijing Key Laboratory of Multiphase Flow and Heat Transfer, North China Electric Power University, Beijing 102206, PR China
[b] Electric Power Department, Beijing Zhongan Quality Assessment Center, Central Technology, Beijing 100022, PR China

ARTICLE INFO

Article history:
Received 4 February 2014
Received in revised form 24 September 2014
Accepted 25 September 2014
Available online 17 October 2014

Keywords:
Helical tube
Centrifugal force
Buoyancy force
Heat transfer coefficient

ABSTRACT

Experiments of carbon dioxide flowing in a helical pipe at near-critical pressure were performed at constant heat flux boundary condition. The helical curvature diameter, helical pitch and tube diameter were 283.0 mm, 32.0 mm and 9.0 mm, respectively. The inlet Reynolds number was larger than 10^4 to ensure the turbulent flow. The renormalization group RNG k–ε model simulated the three-dimensional turbulent heat transfer of CO_2 in the helical pipe. Much attention was paid to the combined effects of the centrifugal force and buoyancy force on the heat transfer. The RNG k–ε model reasonably simulates the complicated heat transfer. The wall temperatures near the tube exit were slightly over-predicted, due to the suppression of the increased wall temperatures near the tube exit by axial thermal conduction in the experiment. Before and near the pseudocritical temperature region, the varied physical properties caused significantly non-uniform velocity and temperature distributions over the tube cross section. The larger axial velocities appear at the outer-bottom location, and the higher wall temperatures appear at the inner-top location. Thus, the outer-bottom locations hold larger heat transfer coefficients. The turbulent kinetic energies are increased along the axial angles and larger in the inner-top region of the tube cross section. The effective viscosities are decreased along the axial angles, and the larger effective viscosities are shifted to the tube center with the axial flow development. Beyond the pseudocritical temperature region, the decreased buoyancy force suppressed the non-uniformity of the heat transfer coefficients over the tube circumference.

1. Introduction

Supercritical fluids have wide applications in air-conditioners, nuclear reactors, supercritical fluid extraction due to their distinct physical properties. Rockets and military aircraft are cooled by fuel at supercritical pressures. Heat is transferred to supercritical water in a modern power plant. Carbon dioxide can be a major alternative refrigerant for automotive air-conditioners and heat pumps due to its good thermodynamic, transport, and environment properties [1]. CO_2 is also considered as a possible working fluid in an Organic Rankine Cycle to recover low grade thermal energy.

The helically-coiled-tube heat exchangers offer several advantages such as simple geometry structure, high heat transfer efficiency and high reliability etc. Many experimental and numerical works have been done on the CO_2 forced convective heat transfer in straight pipes. The studies were performed to investigate the CO_2 forced convective heat transfer in 0.5–2.14 mm inside diameter vertical and horizontal tubes at supercritical pressures (Liao and Zhao [2–4]). The tube was under the heating or cooling boundary conditions. It was found that the inside diameter of the tube had strong effect on the Nusselt number. The numerical simulation demonstrated the important buoyancy force effect on the flow and heat transfer, even for small diameter tubes and large Reynolds number.

Jiang et al. [5–7] conducted experimental and numerical studies on the supercritical pressure CO_2 heat transfer in miniature tubes. The effects of inlet fluid temperatures, pressures, heat fluxes, flow direction, buoyancy force and flow acceleration on the flow and heat transfer were analyzed. The tube wall thickness was found to have small effect on the heat transfer. The heat transfer coefficients were decreased with increases in the inlet fluid pressures.

Bae et al. [8] experimentally investigated the supercritical pressure CO_2 heat transfer in a 6.32 mm inside diameter tube. Several experimental correlations were developed under normal and deteriorated heat transfer conditions. A general deterioration criterion

* Corresponding authors. Tel./fax: +86 10 61772613 (J. Xu). Tel.: +86 10 61772079 (D. Sun).
E-mail addresses: xjl@ncepu.edu.cn (J. Xu), dlsun@ncepu.edu.cn (D. Sun).

http://dx.doi.org/10.1016/j.ijheatmasstransfer.2014.09.066
0017-9310/

Nomenclature

a	radius of the helical pipe, m
A_c	cross section area of the tube, m^2
d	tube diameter, m
D	coil diameter, m
De	dean number
c_p	specific heat, kJ/kg K
g	gravity force (g = 9.81), m/s^2
h	heat transfer coefficient, W/m^2 K
H	specific enthalpy, kJ/kg
k	turbulent kinetic energy, m^2/s^2
L	length of the tube, m
m	mass flow rate, kg/s
Nu	Nusselt number
p	pressure, Pa
q	heat flux, W/m^2
r	radial coordinate, m
R_c	radius of the coil, m
Re	Reynolds number
T_{pc}	pseudocritical temperature, K
T_w	wall temperature, K
$T_{w,x}$	wall temperature, K
u	velocity, m/s
x,y,z	Cartesian coordinate

Greek symbols

δ	curvature ratio
ε	turbulent dissipation rate
φ	axial angle, °
θ	circumferential angle, °
λ	thermal conductivity, W/m K
η	thermal efficiency
μ	dynamic viscosity, Pa s
ρ	density, kg/m^3

Subscripts

b	bulk fluid
eff	turbulent effective parameters
in	inlet condition
pc	pseudocritical
w	wall

was developed to accurately predict the appearance of the heat transfer deterioration.

Du et al. [9] numerically simulated the CO_2 turbulent convective heat transfer in a 6 mm horizontal tube using the FLUENT software. It was found that the simulations using various turbulent flow models could demonstrate the heat transfer characteristic at supercritical pressures. Among these models, the LB-low-Reynolds-number-model matched the experimental data well. The buoyancy force significantly enhances the heat transfer. The buoyancy force is increased to the peak value and then decreased along the flow direction.

Cao et al. [10] numerically simulated the laminar heat transfer of supercritical CO_2 in horizontally circular and triangular channels with cooling boundary conditions. The effects of fluid physical properties and channel geometries on the heat transfer were analyzed. The buoyancy force could enhance the heat transfer near the pseudocritical temperature region. The effect of secondary flow on the heat transfer was analyzed qualitatively. Mao et al. [11] experimentally investigated the supercritical pressure water heat transfer in a helical coiled tube. Over the Reynolds number in the range of 5.5×10^4 to 5.5×10^5, the heat transfer was significantly enhanced due to the apparently changed physical properties of water near the near the pseudocritical temperature region.

To the author's knowledge, there has less studies of turbulent heat transfer to near-critical CO_2 in a helical pipe, which needs to be understood because of its wide applications in power generation systems and reactor facilities. The fluid CO_2 has critical temperature of 31.3 °C and critical pressure of 7.39 MPa, which are significantly lower than water (T_c = 374.2 °C, P_c = 22.114 MPa). The supercritical pressure fluids have varied physical properties versus temperatures, which are more obviously near the pseudocritical temperature region. Due to the varied fluid densities with temperatures, the buoyancy force is generated to induce the secondary flow over the tube cross section. The buoyancy force attains maximum near the pseudocritical temperature point.

In this paper, the experimental data were obtained with CO_2 flowing in a helical tube at the near-critical pressure. The measured data were compared with the numerical simulations to demonstrate the effectiveness of the simulation results. The parameters of velocity, temperature, turbulent kinetic energy and the effective viscosity were carefully analyzed. The wall temperature and heat transfer coefficients were discussed with the effects of buoyancy force and the centrifugal force.

2. The experimental system and data reduction

Fig. 1 shows the experimental setup, including a CO_2 liquid storage tank, a high-pressure piston pump, a mass-flow-meter, a helical tube test section, a condenser, and an expansion valve. The test section was made of a 316L stainless tube. The helical tube had outside and inside diameters of 12.0 mm and 9.0 mm, respectively. The helical curvature diameter was D = 283.0 mm with a pitch distance of 32.0 mm. The maximum axial angle was 2160°, corresponding to six turns of helical coils. The flow was upward and the running pressure was p = 8.0 MPa. The heat was applied on the test tube by applying the alternative voltage on two copper plates. Thus, the constant heat flux boundary condition was assumed. The fluid pressure and differential pressure were measured by the 3051 type pressure and differential pressure transducers, respectively. The pressure and differential pressure had the accuracies of 0.5%. The fluid temperatures and wall temperatures were measured by K-type thermocouples with the accuracy of 0.2 °C. There were 23 cross sections with thermocouple wires welded on the outer wall surface. Each cross section had eight thermocouples. The inside wall temperatures were obtained by the inverse thermal condition solution with known outer wall temperatures [12]. The wall temperatures were non-uniform because of the secondary flow in the tube. The inside wall temperatures were averaged by the eight corresponding temperatures.

$$T_w = \left(\sum_{i=1}^{8} T_{wi}\right) \Big/ 8 \tag{1}$$

where T_{wi} was the inside wall temperature computed by the inverse heat condition solution.

Along the axial flow direction, there were 23 cross sections on which thermocouples were welded. The bulk fluid temperature at ach cross section was determined by the fluid enthalpy at the local pressure. The NIST (Standard Reference Database 23 (REFPROP Version 8.0) [13] helped to decide the value at specific enthalpy and pressure. The fluid enthalpy was obtained as

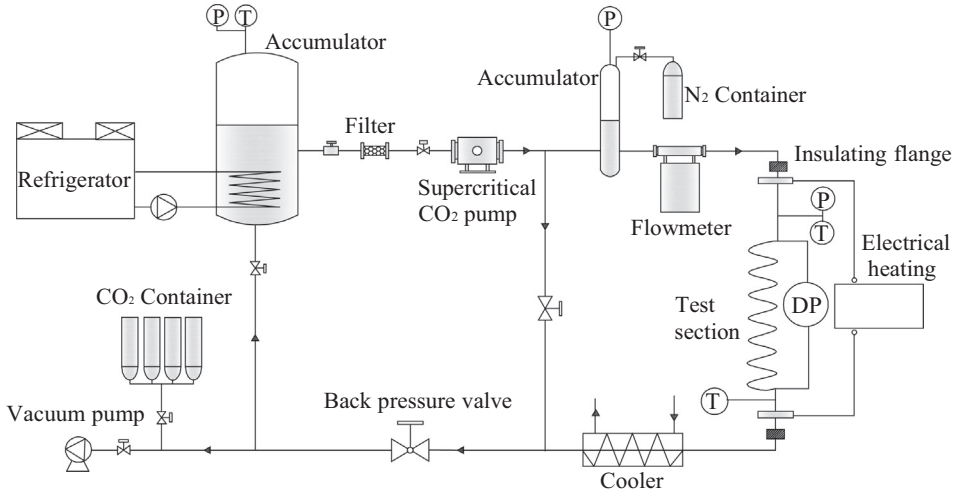

Fig. 1. The experimental setup for CO_2 forced convective heat transfer in helical pipes.

$$H_b = H_{in} + \frac{l_c}{L}\frac{\eta q_w A_c}{m_{in}} \tag{2}$$

where H_b was the bulk fluid enthalpy, H_{in} was the inlet enthalpy, l_c was the distance from the cross section c to the local position, L was the total heating length, L = 5.5 m, m_{in} was the mass flow rate, η was the thermal efficiency, q_w was the heat flux at the inside wall surface, A_c was the cross sectional area. The maximum temperature difference over the tube cross section was decided as

$$\Delta T = T_{wi,\max} - T_{wi,\min} \tag{3}$$

where $T_{wi,\max}$ and $T_{wi,\min}$ were the maximum and minimum inside wall temperatures, respectively.

3. The numerical simulation

3.1. The physical model

Dean [14] computed the flow field in a helical pipe with smaller helical coil curvature. He defined the *De* number as $De = Re\sqrt{a/R_c}$ to characterize the intensity of the centrifugal force, where *Re* is the Reynolds number, a is the tube radius and R_c is the curvature radius of the helical coil. Many studies showed that the helical curvature influences the centrifugal force to from the secondary flow, and the helical pitch influences the torsional force.

Fig. 2 shows the helically coiled tube for both the numerical simulation and experimental studies. The helical pipe curvature ratio δ was defined as the tube radius (a) divided by the helical pipe coil radius (R_c). The CO_2 fluid flows from inlet to outlet. The flow was turbulent. The secondary flow can be generated by the centrifugal force and buoyancy force to have non-uniform parameter distribution over the tube cross section. The top, bottom, inner and outer generatrix locations were marked in Fig. 2. The physical properties of CO_2 were varied along the flow direction and over the tube cross section. The secondary flow over the tube cross section delays the transition from laminar flow to turbulent flow. The transition point is usually difficult to be determined in helical pipes, but may be estimated by the following four correlations:

The critical Reynolds number proposed by Ito [15] (1959):

$$Re_{cr} = 2 \times 10^4 \times \delta^{0.32} \tag{4}$$

The critical Reynolds number proposed by Schmidt [16] (1967):

$$Re_{cr} = 2300 \times (1 + 8.6\delta^{0.45}) \tag{5}$$

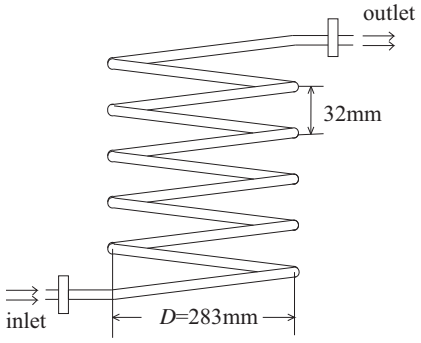

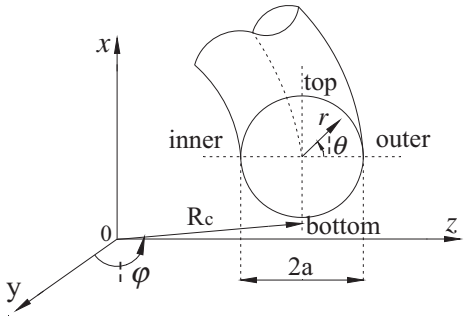

Fig. 2. The helical pipe and its coordinate system.

The critical Reynolds number proposed by Srinivasan et al. [17] (1970):

$$Re_{cr} = 2100 \times (1 + 12\delta^{0.5}) \tag{6}$$

where δ is in the range of $(9.7 \times 10^{-3}, 0.135)$.

Jasson and Hoogendoorn [18] proposed the following critical Reynolds number in 1978:

$$Re_{cr} = 2400 \times (1 + 16.46\delta^{0.68}) \tag{7}$$

where $\delta = a/R_c$.

In this study, δ is equal to 0.03. The critical Reynolds number was 6512, 6040, 6465 and 6383 using the above four correlations.

Therefore, *Re* should be greater than 6000 to ensure the turbulent flow in the present helical pipe. The present experimental and numerical simulation had the Reynolds number in the range of (10,290–27,581).

3.2. The governing equations

There are five turbulent flow models embedded in the FLUENT software [19]. The RNG k–ε model [20] simulated the turbulent heat transfer in the helical pipe because the RNG model includes an additional term in its equation that improves the accuracy for rapidly strained flows, such as those in helical pipes. All the physical properties (density, specific heat, enthalpy, etc) were changed in terms of pressures and temperatures. Similar turbulent model was used by Li et al. [21] to simulate the near-critical water heat transfer in helical pipes. The governing equations were solved in the Cartesian coordinate system, which were written as

Mass:

$$\frac{\partial(\rho u_i)}{\partial x_i} = 0 \tag{8}$$

Momentum:

$$\frac{\partial(\rho u_i u_j)}{\partial x_j} = -\frac{\partial p}{\partial x_i} + \rho g_i + \frac{\partial}{\partial x_j}\left[\mu_{eff}\left(\frac{\partial u_i}{\partial x_j} + \frac{\partial u_j}{\partial x_i}\right) - \frac{2}{3}\mu_{eff}\frac{\partial u_k}{\partial x_k}\right] \tag{9}$$

Energy:

$$\frac{\partial(\rho u_i c_p T)}{\partial x_i} = \frac{\partial}{\partial x_i}\left[\alpha_T\left(\mu_{eff}\frac{\partial T}{\partial x_i}\right)\right] + \frac{\partial u_i}{\partial x_j}\left[\mu_{eff}\left(\frac{\partial u_i}{\partial x_j} + \frac{\partial u_j}{\partial x_i}\right) - \frac{2}{3}\mu_{eff}\frac{\partial u_k}{\partial x_k}\delta_{ij}\right] \tag{10}$$

Turbulent kinetic energy:

$$\frac{\partial(\rho u_i k)}{\partial x_i} = \frac{\partial}{\partial x_i}\left[\alpha_k \mu_{eff}\frac{\partial k}{\partial x_i}\right] + G_b + \mu_t S^2 + \rho\varepsilon \tag{11}$$

Dissipation rate of turbulent kinetic energy:

$$\frac{\partial(\rho u_i \varepsilon)}{\partial x_i} = \frac{\partial}{\partial x_i}\left[\alpha_k \mu_{eff}\frac{\partial \varepsilon}{\partial x_i}\right] + C_{1\varepsilon}\frac{\varepsilon}{k}\mu_t S^2 + C_{2\varepsilon}\rho\frac{\varepsilon^2}{k} - R \tag{12}$$

The effective viscosity, μ_{eff}, was computed by the following equation:

$$\mu_{eff} = \mu_{\mathrm{mol}}\left(1 + \sqrt{\frac{C_\mu}{\mu_{\mathrm{mol}}}}\frac{k}{\sqrt{\varepsilon}}\right)^2 \tag{13}$$

where μ_{mol} is the molecular viscosity. The coefficients α_T, α_k and α_ε are the inverse effect Prandtl numbers for T, k and ε, respectively. They were calculated according to the correlation of

$$\left|\frac{\alpha - 1.3929}{\alpha_0 - 1.3929}\right|^{0.6321}\left|\frac{\alpha + 2.3929}{\alpha_0 + 2.3929}\right|^{0.3679} = \frac{\mu_{mol}}{\mu_{eff}} \tag{14}$$

where α_0 equals to $1/Pr$, 1.0 and 1.0 for the computation of α_T, α_k and α_ε.

In the RNG k–ε model, the coefficients of buoyancy force on the turbulence can be considered by G_b, which is written as

$$G_b = -g_i\alpha_T\mu_t\frac{1}{\rho}\frac{\partial T}{\partial x_i}\left(\frac{\partial \rho}{\partial T}\right)_p \tag{15}$$

S in Eqs. (11) and (12) is the modulus of the mean rate-of-strain tensor, which is defined as

$$S = \sqrt{2S_{ij}S_{ij}} \tag{16}$$

where $S_{ij} = \frac{1}{2}\left(\frac{\partial u_i}{\partial x_j} + \frac{\partial u_j}{\partial x_i}\right)$, R in Eq. (12) was computed as

$$R = \frac{C_\mu\rho\eta^3(1-\eta/\eta_0)}{1+\zeta\eta^3}\frac{\varepsilon^2}{k} \tag{17}$$

where $\eta = Sk/\varepsilon$, $\eta_0 \approx 4.38$, $\zeta = 0.012$. The constants get the following values: $C_\mu = 0.085$, $C_{1\varepsilon} = 1.42$, $C_{2\varepsilon} = 1.68$.

The fluid bulk temperature T_b was averaged over each cross section, written as

$$T_b = \frac{1}{A_c}\int_{A_c} T_i dA \tag{18}$$

The wall heat transfer coefficient was defined as

$$h = \frac{q_w}{T_w - T_b} \tag{19}$$

Note that h can be the local value or the wall averaged value, corresponding to the local wall temperature or the circumference averaged wall temperature used, respectively.

3.3. The grid generation and boundary conditions

The turbulent mixed convective heat transfer in the helical pipe was solved by the FLUENT software. The mass, momentum, energy and k–ε equations are solved by the control-volume-finite-element-volume (CVFEM) method. The three-dimensional flow and heat transfer were computed with emphasis on the centrifugal force and buoyancy force. The pipe wall thickness was assumed to be zero.

The SIMPLEC algorithm resolved the coupling between velocity and pressure. The second-order upwind scheme was used for the discretization of convection terms in the governing equations, while the diffusion term was computed by means of multi-linear interpolating polynomials. The Skewness correction value was set be one. Due to the large variation of the fluid physical properties, the under-relaxation factors ranged from 0.1 to 0.3 for all independent variables. The maximum residual values for the mass equation and for the momentum and energy equations were less than 1.0×10^{-4} and 1.0×10^{-6}, respectively. The computations were assumed to be converged when the outlet mass flow rate was exactly the same as the inlet value, and the residual curves versus time do not change anymore.

The unstructured grid generation system was used, with fine grids near the tube wall and relatively coarse grids in the bulk flow region. The number of grids influence the computation results. The sensitivity of grid number was examined. The total number of grids was 2.52 million. Further refinement of the grids had no improvement of the computation results.

The inlet CO_2 pressure was 8.0 MPa. The inlet mass flow rate and fluid temperature were set as constant values. The inlet boundary conditions involved the following parameters: $I = 0.16Re^{-1/8}$ for the turbulent intensity, $k_{in} = 1.5(u_{in}I)^2$ for the turbulent kinetic energy, and $\varepsilon_{in} = C_\mu^{3/4}k_{in}^{3/2}/l$ for the dissipation rate of turbulent kinetic energy, where l is the characteristic length ($l = 0.07d$, where d is the pipe diameter and $d = 9.0$ mm here).The pipe outlet used the free boundary condition. The nonslip boundary condition was applied on the tube wall. The wall received the constant heat flux. The enhanced wall function was applied near the tube wall. The y^+ value corresponding to the first grid layer thickness near the wall should be smaller than one, which was satisfied in this study.

Fig. 3 shows the physical properties of CO_2 at the pressure of 8.0 MPa, noting that the critical pressure is 7.39 MPa. These properties were cited from the NIST Standard Reference Database 23 (REFPROP Version 8.0) [13]. The thermal capacity, c_p, reached the maximum value at the pseudocritical temperature of 307.6 K at $p = 8.0$ MPa. The physical properties of CO_2 in terms of temperatures were incorporated in the computation via the piecewise-liner input.

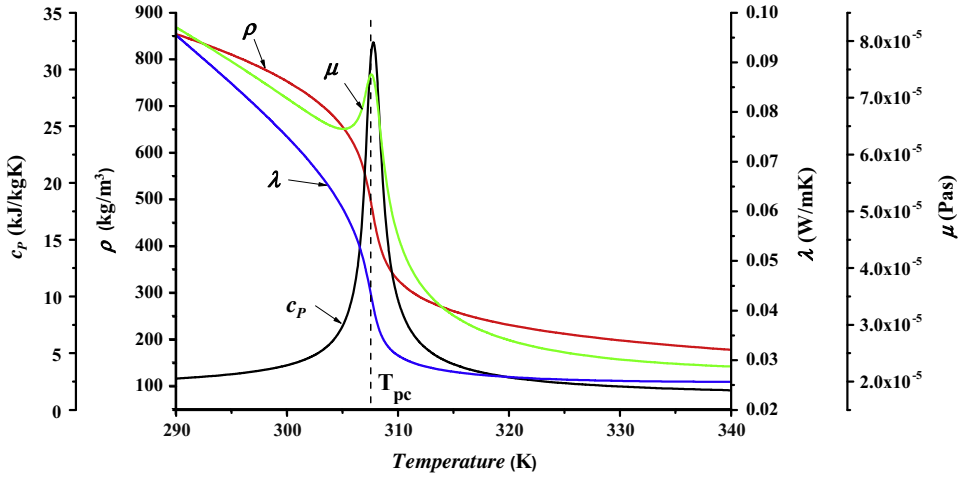

Fig. 3. The physical properties of CO_2 at 8.0 MPa.

4. Results and discussion

4.1. The experimental data and comparison with the numerical simulation

Table 1 shows nine cases performed at $g = 9.80\ m/s^2$. The inlet Reynolds numbers are larger than 10^4 to ensure the turbulent flow in the helical pipe. Cases 1–3 were performed at the same heat flux ($q = 20.5\ kW/m^2$), but the mass flow rates are increased from case 1 to case 3. Alternatively, cases 4–6 were performed at the same mass flow rate ($m_{in} = 6.23\ g/s$), but the heat fluxes are increased from case 4 to case 6. Case 7 was arranged for the comparison between the measurements and numerical simulations. Case 8 was compared with case 9, in which case 8 is for the adiabatic flow (no buoyancy force effect), and case 9 is with heat transfer (buoyancy force effect). Flow and heat transfer characteristics were carefully discussed for case 9.

Fig. 4 shows the peripherally averaged wall temperatures (black symbols) and the fluid bulk temperatures (red symbols) versus the axis angle positions for cases 1–3. Due to the continuous heating, the wall temperatures are higher than the bulk fluid temperatures at the same axial location. The wall temperatures and fluid temperatures are decreased with increases in the mass flow rates.

Fig. 5 illustrates the peripherally averaged wall temperatures (black symbols) and the bulk fluid temperatures (red symbols) for cases 4–6. They showed the rise trend along the flow direction. It is found that case 4 behaves the smallest difference between the wall temperature and the bulk fluid temperature due to the small heat flux of $1.65\ kW/m^2$. The outlet CO_2 temperature is less than the pseudocritical temperature, T_{pc}. The cases 5 and 6 had faster increase trend of T_w and T_b along the axial angle position. Both of T_w and T_b at the outlet plane are larger than T_{pc}.

Table 1
Run parameters for the present experiment and computations.

Cases	m_{in} (kg/s)	T_{in} (K)	q_w (kW/m²)	Re_{in}	De	Gravity force
1	1.31×10^{-2}	287.05	20.5	21,636	3858	g
2	1.51×10^{-2}	287.86	20.5	24,939	4447	g
3	1.67×10^{-2}	287.88	20.5	27,581	4919	g
4	6.23×10^{-3}	287.15	1.65	10,290	1835	g
5	6.23×10^{-3}	287.53	9.03	10,290	1835	g
6	6.23×10^{-3}	287.66	12.13	10,290	1835	g
7	8.94×10^{-3}	287.04	16.0	14,725	2550	g
8	7.08×10^{-3}	298.15	0	15,000	2598	g
9	7.08×10^{-3}	298.15	10.0	15,000	2598	g

Fig. 6 shows the measured wall temperatures for case 7, in which Fig. 6a shows the circumference angle (θ). The whole helical coiled tube had 23 cross sections with eight thermocouples uniformly distributed on the tube wall. Fig. 6b shows the wall

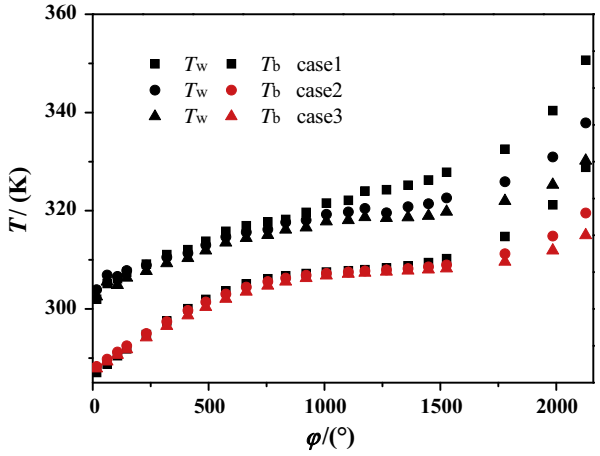

Fig. 4. The wall and bulk fluid temperatures along the axial angles (cases 1–3).

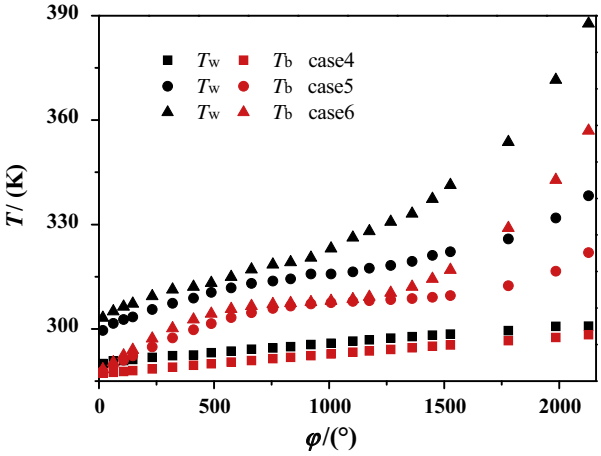

Fig. 5. The wall and bulk fluid temperatures along the axial angles (case 4–6).

temperature distributions along the circumference angles (θ) at different axial angles φ. It was found that with $\varphi < 660°$, the wall temperatures were decreased and then increased with θ from 0° to 360°. The minimum wall temperatures occurred at $\theta = 135°$ (the outer-bottom location). The maximum wall temperature occurred at the top location ($\theta = 0°$). When φ was in the range of $660° < \varphi < 1572°$, the wall temperatures were decreased, then increased and further decreased, with θ changed from 0° to 360°. The minimum wall temperature appeared at $\theta = 95°$. Fig. 6c shows the non-dimensional temperature difference over each tube cross section along the axial flow coordinate. The specific heat variation was also plotted. It was found that the dimensionless temperature differences were increased, attained maximum near the pseudo-

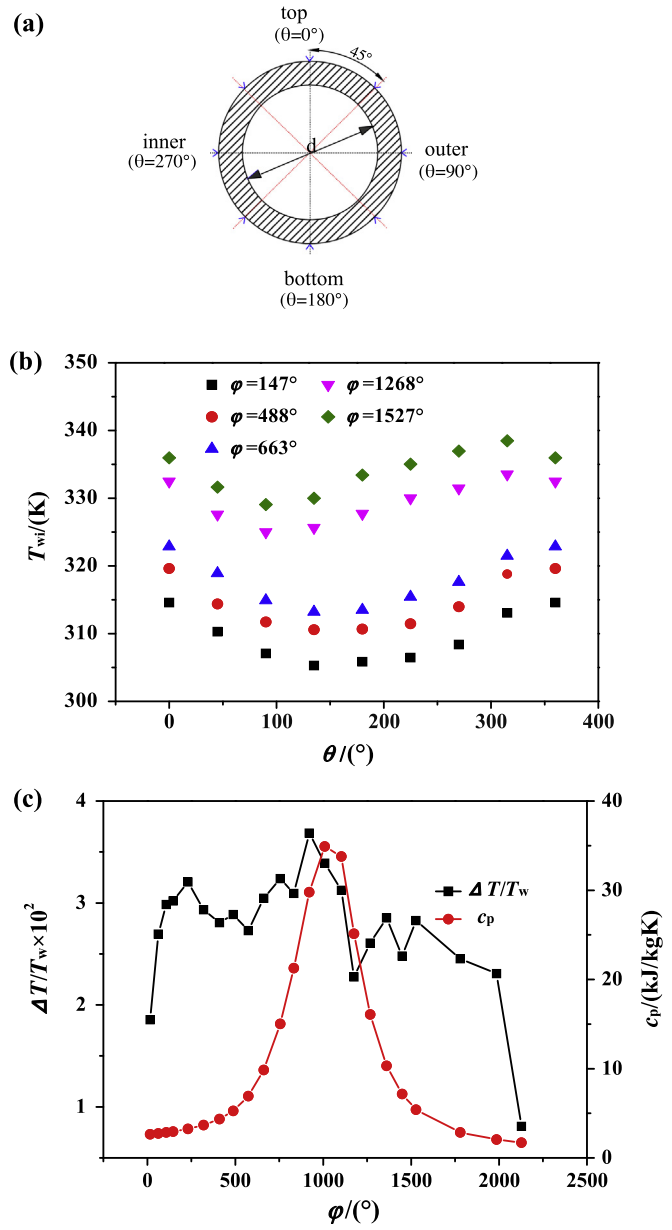

Fig. 6. The wall temperature and its non-uniformity along the axial angle and circumference angle (case 7).

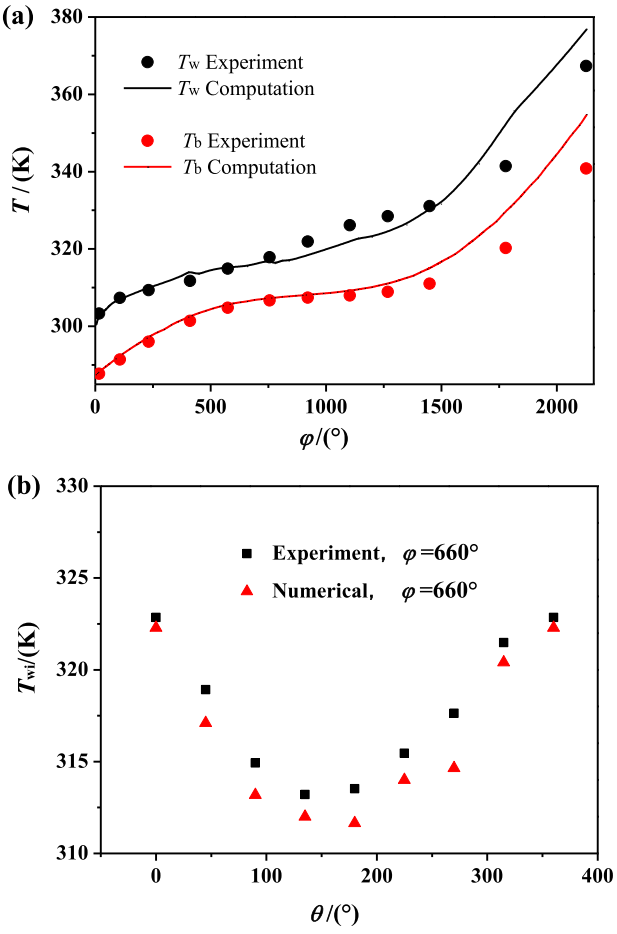

Fig. 8. The comparison between the measurements and numerical simulation for case 7 (a: the wall averaged temperatures along the axial angles, b: the wall temperature distribution along the circumference angles).

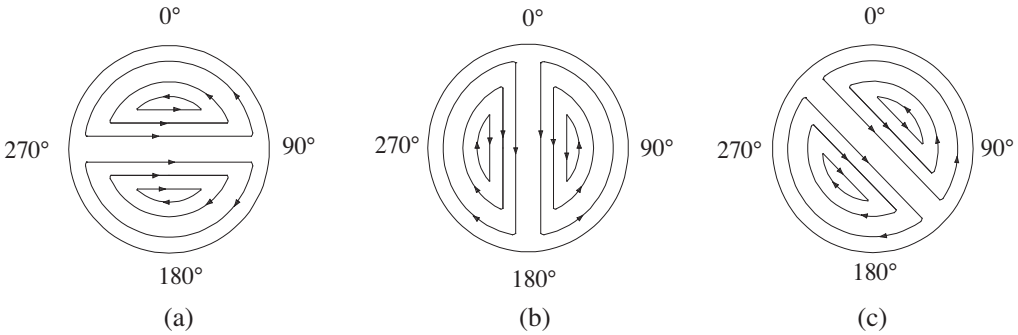

Fig. 7. Flow patterns over the tube cross section (a: only the centrifugal force effect, b: only the buoyancy force effect, and c: the combined force effect).

critical temperature region and then decreased. The sharp change of specific heats near the pseudocritical temperature region enhanced the temperature variations over the tube cross section. The above phenomenon was caused by the combined effects of buoyancy force and centrifugal force. Fig. 7 shows the possible three flow patterns over the tube cross section. Fig. 7a shows the flow pattern with only the centrifugal force effect. The heavy fluid with lower temperature is populated in the tube outer region and light fluid with higher temperature is populated in the tube inner region. This situation happens in helical tube with normal fluid physical properties. Fig. 7b shows the flow pattern influenced by the buoyancy force only, with heavy fluid at the bottom and light fluid at the top locations. This situation happens in a straight horizontal tube with supercritical pressure fluid having varied densities. Fig. 7c gave the flow pattern for flow just like supercritical pressure CO_2 flowing in helical coiled tube, reflecting the combined effect of centrifugal force and buoyancy force. This explained why the minimum wall temperature occurred in the outer-bottom region.

Because there is no data on the turbulent mixed convective heat transfer to near-critical CO_2 in a helical pipe, our experimental data were compared with the numerical simulations to verify the model effectiveness. Fig. 8a shows the comparison between the measurements and the simulation results for case 7, in which solid symbols and solid curves represented the experimental data and simulation results, respectively. The agreement is excellent for axial angle $\varphi < 1500°$. The numerical simulation slightly over-predicted the wall and bulk fluid temperatures for the last two points, due to the fact that the axial thermal conduction suppressed the temperature rise near the tube exit, in the experiment. Meanwhile, Fig. 8b shows the correct simulation trend of wall temperatures along the circumference direction, compared with the temperature measurements. The difference between measurements and simulations for each point was about 1 °C.

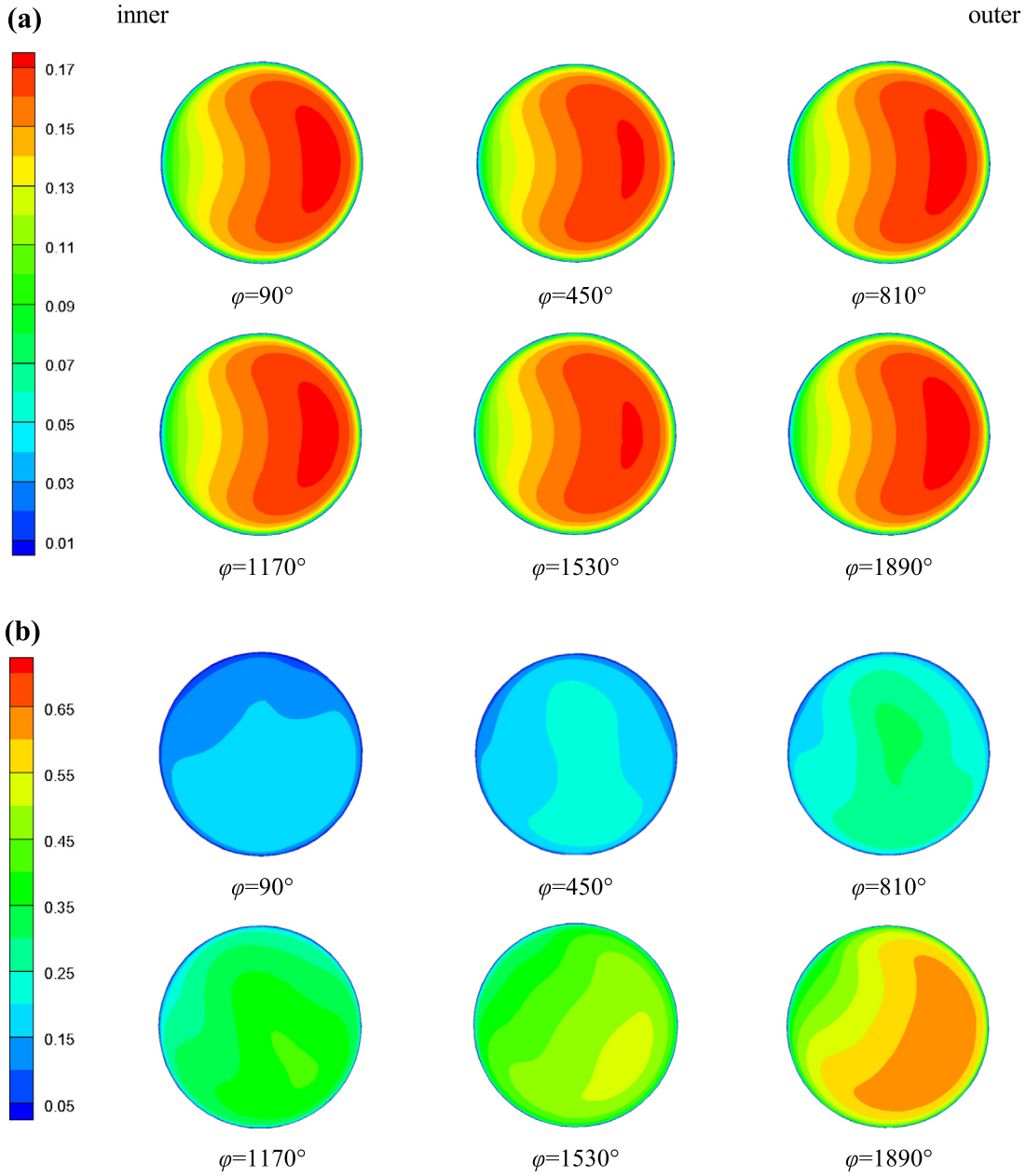

Fig. 9. The velocity isotachs for case 8 (a) and case 9 (b).

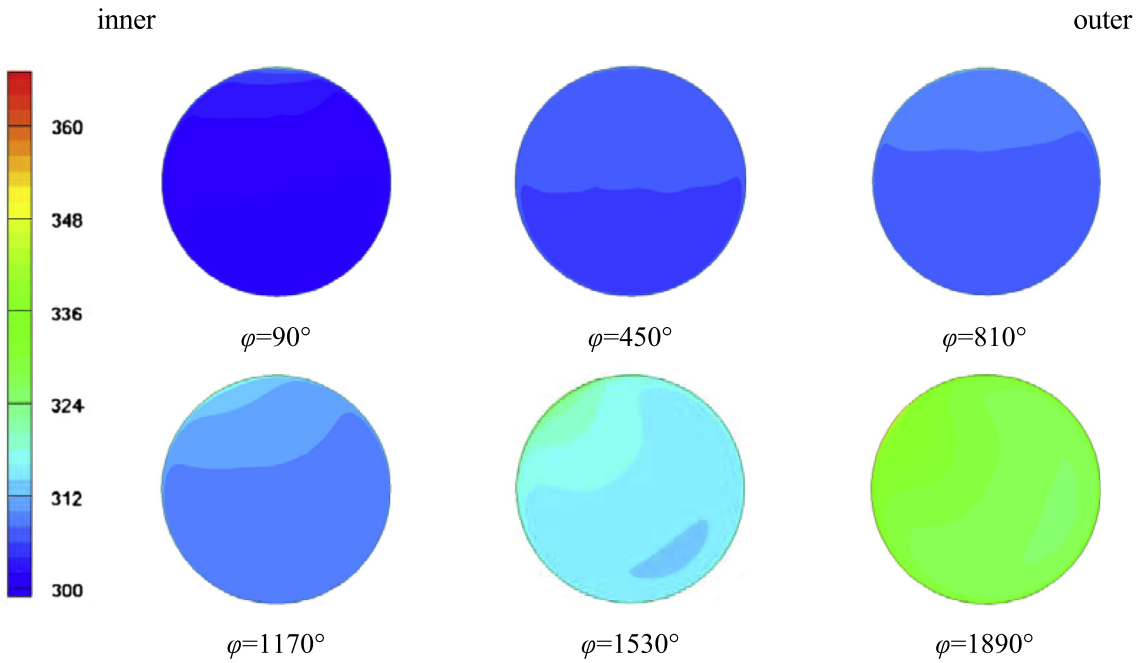

Fig. 10. The isotherms for the case 9.

4.2. The velocity and temperature distributions

Fig. 9a shows the velocity isotachs for case 8 ($q = 0$, adiabatic flow). The flow becomes fully developed for $\varphi > 90°$. Because there is no buoyancy force, the isotachs are symmetric from the top to bottom. But the flow is strongly non-symmetric from inner to outer side. The centrifugal force creates larger velocities at the outer side than the inner side. Fig. 9b represented the combined influence of the buoyancy force and centrifugal force on isotachs. The CO_2 fluid has been accelerating along the axial angle due to continuous heating. By comparing case 8 with case 9, one found that the buoyancy force makes the larger velocities appearing in the outer-bottom region of the tube cross section. The movement of larger velocities from the outer region (adiabatic flow) to the outer-bottom region (heating condition) is due to the buoyancy force effect by the density variations over the tube cross section.

Correspondingly, Fig. 10 illustrates the isotherms for case 9 (heating condition). The non-uniformity of the fluid temperatures is enhanced along the axial angle. The temperatures near the tube wall are higher than those in the tube core. The buoyancy force creates higher temperatures in the top region. On the other hand, the centrifugal force generates higher temperatures in the inner side. Therefore, the combined effect yields higher temperatures occurring in the inner-top region of the tube cross section. This phenomenon is more obvious at $\varphi = 1170°$.

Fig. 11 shows the dimensionless axial velocities (u/u_{in}) over the tube radius (r/a, where a is tube radius), in which the solid curves are on the vertical line from bottom ($r/a = -1$) to top ($r/a = 1$), and the dashed curves are on the horizontal line from inner ($r/a = -1$) to outer ($r/a = 1$). Thus, the solid and dashed curves reflect the effects of the buoyancy force and the centrifugal force on the axial velocities, respectively. The fluid is being accelerated versus the axial angles. The apparently non-symmetric distribution of u/u_{in} was identified on the vertical line due to the buoyancy force effect for $\varphi = 90°$ (14 turn of the helical coil) and 360° (a full turn of the helical coil). The maximum axial velocity occurs near the tube bottom at the two axial angles. This symmetric behavior is improved at $\varphi = 900°$ (2.5 turns of the helical coil), at which the maximum axial velocity appears at the tube center ($r/a = 0$). Meanwhile, the

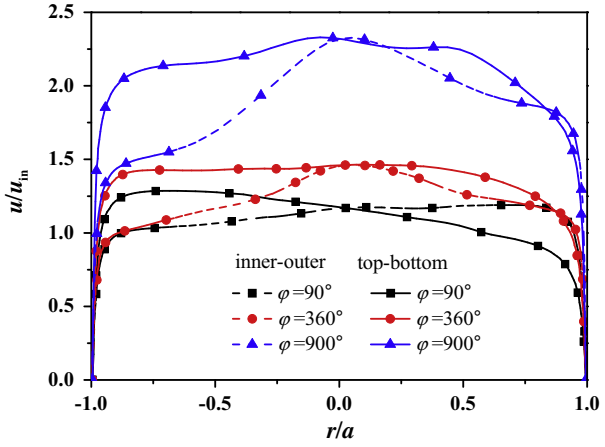

Fig. 11. The axial velocity versus r/a for case 9.

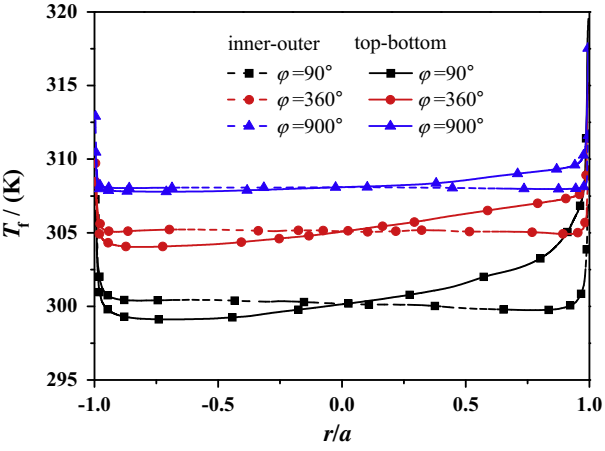

Fig. 12. The fluid temperatures versus r/a for the case 9.

centrifugal force generates larger velocities at the outer side than the inner side. This non-symmetric characteristic happens for all the axial angles φ.

Fig. 12 illustrates the CO_2 fluid temperatures on the vertical and horizontal lines. At the heating condition, the fluid temperatures are largest at the wall surface and sharply decreased near the tube wall. The sharply decreased temperature region is called the thermal boundary layer near the tube wall. The fluid temperatures are gradually increased along the flow direction at the constant heat flux boundary condition. It is seen that the temperatures are symmetrically distributed against $r/a = 0$ from inner to outer sides. However, the temperatures are gradually increased from bottom to top. The fluid temperatures are raised from the bottom to top. This is caused by the density variation over the vertical coordinate to yield the secondary flow. The lighter fluid with higher temperatures are populated at the top but the heavier fluid with lower temperatures are populated at the bottom. Again, it is seen that the fluid temperatures are lower at the outer side than the inner side. The centrifugal force creates the heavy fluid with lower temperatures happening at the outer side.

4.3. The turbulent kinetic energy and effective viscosity

Fig. 13 shows the turbulent kinetic energy (k) at different axial angles (φ). The k values are largest near the tube wall and sharply reduced in the bulk cross section. The k values are also increased with increases in the axial angles, φ. The non-uniformity characteristic of the k distribution is enhanced with flow downstream. For instance, the larger k values are populated in the top-inner region of the cross section at $\varphi = 1890°$. Generally, the k distribution follows the fluid temperature distribution (see Fig. 10). The effective viscosity μ_{eff} distribution (see Fig. 14) is quite different

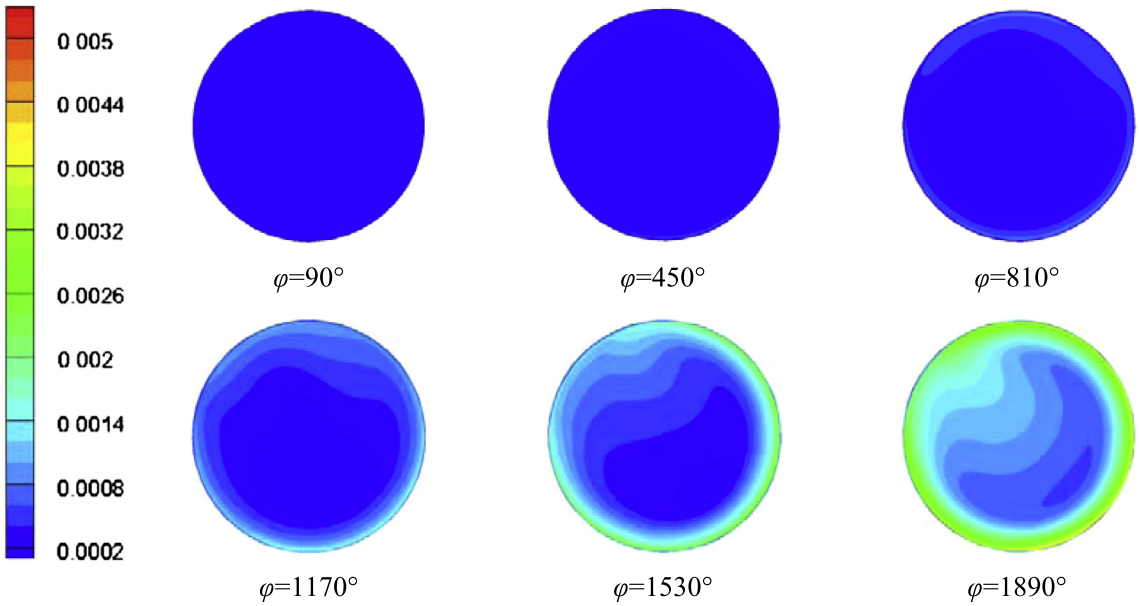

Fig. 13. The turbulent kinetic energy distribution at different axial angles for the case 9.

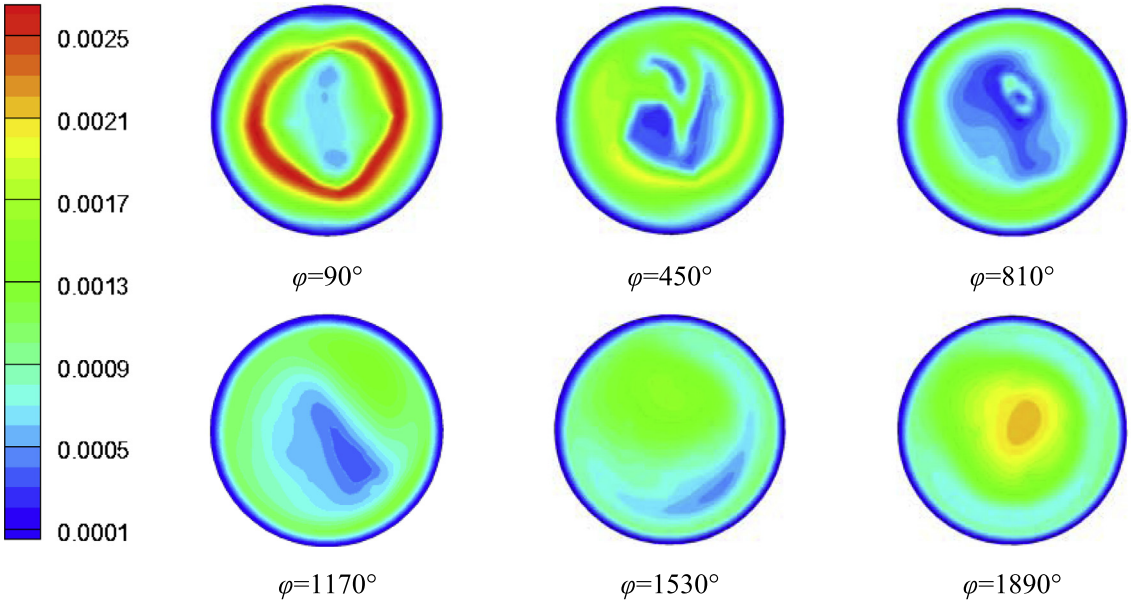

Fig. 14. The effective viscosity at different axial angles for the case 9.

from the k distribution. At the tube entrance such as $\varphi = 90°$ (1/4 turn of the helical coil), the maximum μ_{eff} takes place in the area between the tube wall and the center (see the red O-ring area for $\varphi = 90°$ in Fig. 14). The larger μ_{eff} area gradually moves to the tube center, which is obvious for $\varphi = 1890°$ (see the last pattern in Fig. 14).

Correspondingly, the turbulent kinetic energy k distribution is plotted against the tube radius in Fig. 15. The four axial angle positions of $\varphi = 90°$, 360° and 900° are focused on. The k distribution displays the quasi-symmetric behavior against $r/a = 0$. The peak value appears near the tube wall. Fig. 13 tells us the non-symmetric k distribution against $r/a = 0$ for the downstream flow such as $\varphi > 1170°$. Fig. 16 gave the μ_{eff} distribution against $r/a = 0$, which is a typical double-peak distribution. The increased fluid temperatures gradually reduced the effective viscosities along the axial flow direction. Fig. 14 tells us that the downstream flow moves the peak (or maximum) μ_{eff} locations to the tube center.

4.4. The wall temperatures and heat transfer coefficients

The peripherally averaged heat transfer coefficients are typically illustrated along the axial angles in Fig. 17. The cases 7 and 9 are selected for the presentation (see Table 1). The two cases had different mass flow rates and heat fluxes, but the inlet Reynolds numbers are almost the same. They behave the similar

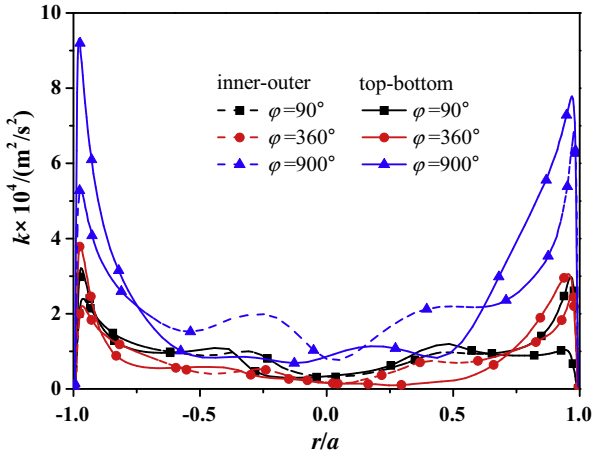

Fig. 15. The turbulent kinetic energy versus r/a for the case 9.

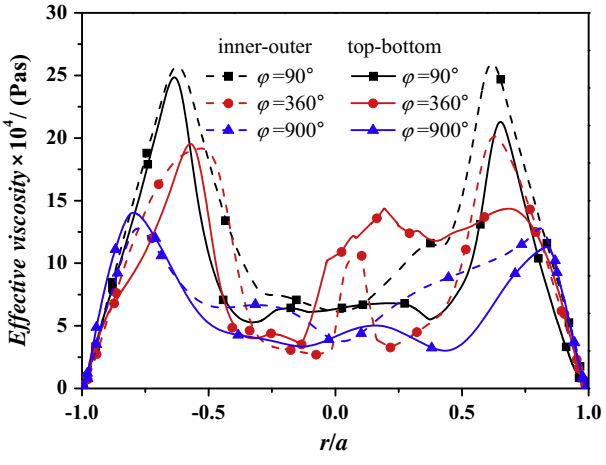

Fig. 16. The effective viscosity versus r/a for the case 9.

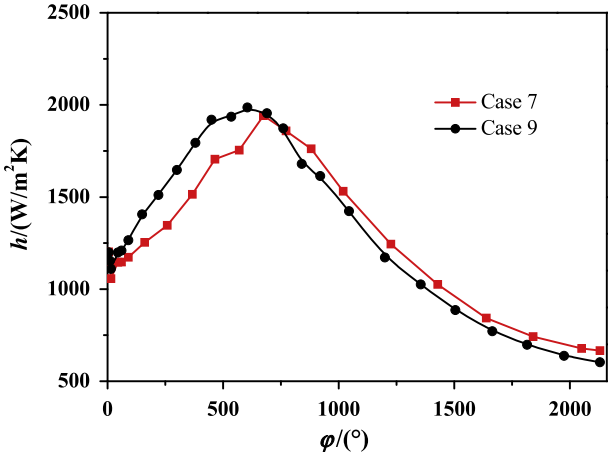

Fig. 17. The averaged heat transfer coefficients along the axial angles for the case 9.

heat transfer coefficient distribution. For the initial a couple of turns, the heat transfer coefficients, h, show the increase trend. The h values attains the maximum value at around $\varphi = 720°$ (two turns of the helical coil), and then decreased. The axial h distribution is strongly related to the secondary flow intensity over the tube cross section. The maximum h values takes place near the pseudocritical temperature, at which the density and specific heat are very sensitive to the temperature variations, yielding the strong secondary flow intensity to enhance the heat transfer. Further beyond the pseudocritical temperature, the physical properties are less influenced by the fluid temperatures, and the intensity of the secondary flow in the tube cross section is weakened to gradually decrease the heat transfer coefficients.

Fig. 18 shows the wall temperatures at the top, bottom, inner and outer generatrices. At the constant heat flux boundary condition, the wall temperatures reflect the heat transfer coefficients (see Fig. 19). The wall temperatures are larger than the bulk fluid temperatures, and they are all increased with increases in the axial angles. The non-uniform wall temperatures over the tube circumference were identified, which are verified by the present experimental measurements. The bottom and outer generatrices share similar and lower wall temperatures. The wall temperatures at the top generatrix are intercrossed with those at the inner generatrix at the axial location of $\varphi = 1500°$, indicating the strong buoyancy force effect before four turns of the helical coil. Beyond the crossing point of $\varphi = 1500°$, the dominant mechanism returns to

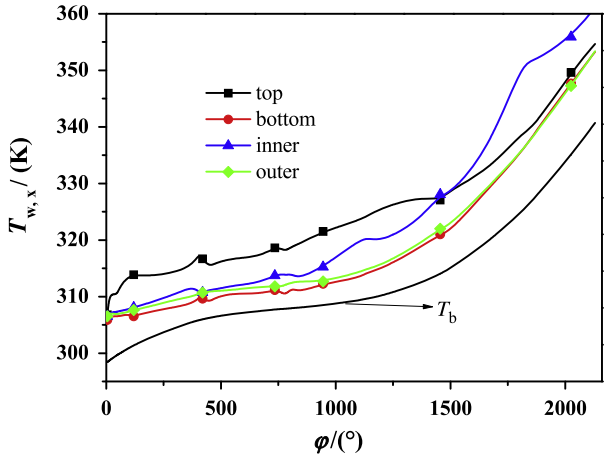

Fig. 18. The local wall temperatures along the axial angles for the case 9.

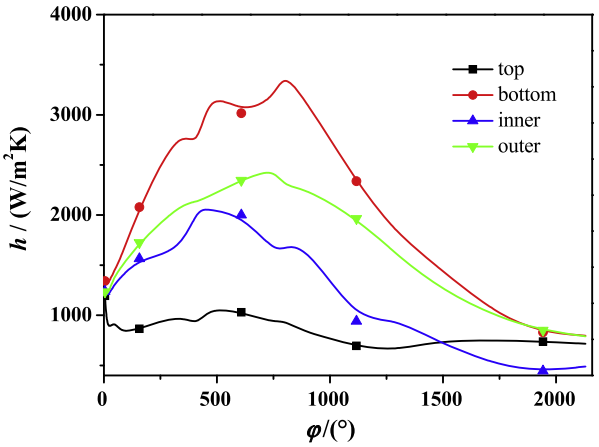

Fig. 19. The local heat transfer coefficients along the axial angles for the case 9.

the centrifugal force effect on the heat transfer. The heat transfer coefficients at the four generatrices were shown in Fig. 19. The bottom generatrix had the largest heat transfer coefficients over the tube cross section. The heat transfer coefficients on the top generatrix are less varied along the axial positions, compared with other locations. The inner and outer generatrices had the heat transfer coefficients larger than the top generatrix but smaller than the bottom generatrix. Corresponding to the wall temperature distribution (see Fig. 18), the heat transfer coefficients had the crossing point at $\varphi = 1500°$ for the top and inner generatrices (see Fig. 19).

Figs. 18 and 19 show the fluctuations of wall temperatures and local heat transfer coefficients. The possible reason is the heating caused density variations along the flow direction and over the tube cross section. The density variation further results in the velocity fluctuation and mass flow rate fluctuation. However, the mass flow rate at the tube inlet is constant. This feedback effect suppresses the growth of the fluctuations. Thus, the amplitude of the fluctuations is limited and the fluctuation happens locally.

5. Conclusions

The experimental and numerical investigations were performed with carbon dioxide flowing in a helical pipe at near-critical pressure. The constant heat flux boundary condition was applied. The inlet Reynolds number was larger than 10^4 so that the turbulent flow was involved. The RNG k–ε turbulent model simulated the three-dimensional flow and heat transfer of CO_2 in the helical pipe. It was found that the numerical simulations agreed with the experimental measurements well.

The combined effects of the buoyancy force and centrifugal force cause the peculiar distribution of the flow and heat transfer parameters over the tube cross section. The present study identified the larger axial velocities in the outer-bottom region. Correspondingly, the larger heat transfer coefficients are also populated there. The inner-top region possesses the higher fluid temperatures over the tube cross section.

The turbulent kinetic energies and effective viscosities are increased and decreased along the axial angles, respectively. Both the two parameters display the double-peak distributions versus the tube radius from top to bottom and from inner to outer. The larger effective viscosities are shifted to the tube center for the axial downstream flow. The near-pseudocritical temperature region enhances the non-uniformity of these parameters. Beyond the pseudocritical temperature region, the centrifugal force dominates the heat transfer and the buoyancy force has less effect to weaken the non-uniformity of the flow and heat transfer parameters.

Conflict of interest

None declared.

Acknowledgements

This work was supported by the Natural Science Foundation of China of international cooperation project (51210011), and by the Natural Science Foundation of China (51006035 and U1034004).

Reference

[1] P.X. Jiang, C.R. Zhao, R.F. Shi, Y. Chen, W. Ambrosini, Experimental and numerical study of convection heat transfer of CO_2 at super-critical pressures during cooling in small vertical tube, Int. J. Heat Mass Transfer 52 (2009) 4748–4756.
[2] S.M. Liao, T.S. Zhao, Measurements of heat transfer coefficients from supercritical carbon dioxide flowing in horizontal mini-micro channels, J. Heat Transfer 24 (2002) 413–420.
[3] S.M. Liao, T.S. Zhao, An experimental investigation of convection heat transfer to supercritical carbon dioxide in miniature tubes, Int. J. Heat Mass Transfer 45 (2002) 5025–5034.
[4] S.M. Liao, T.S. Zhao, A numerical investigation of laminar convection of supercritical carbon dioxide in vertical mini/micro tubes, Prog. Comput. Fluid Dyn. 2 (2002) 144–152.
[5] P.X. Jiang, Y. Zhang, R.F. Shi, Experimental and numerical investigation of convection heat transfer of CO_2 at supercritical pressures in a vertical mini-tube, Int. J. Heat Mass Transfer 51 (2008) 3052–3056.
[6] P.X. Jiang, Y. Zhang, C.R. Zhao, R.F. Shi, Convection heat transfer of CO_2 at supercritical pressures in a vertical mini tube at relatively low Reynolds numbers, Exp. Therm. Fluid Sci. 32 (2008) 1628–1637.
[7] Z.H. Li, P.X. Jiang, C.R. Zhao, Y. Zhang, Experimental investigation of convection heat transfer of CO_2 at supercritical pressures in a vertical circular tube, Exp. Therm. Fluid Sci. 34 (2010) 1162–1171.
[8] Y.Y. Bae, H.Y. Kim, D.J. Kang, Forced and mixed convection heat transfer to supercritical CO_2 vertically flowing in a uniformly-heated circular tube, Exp. Therm. Fluid Sci. 34 (2010) 1295–1308.
[9] Z.X. Du, W.S. Lin, A.Z. Gu, Numerical investigation of cooling heat transfer to supercritical CO_2 in a horizontal circular tube, J. Supercrit. Fluids 55 (2010) 116–121.
[10] X.L. Cao, Z.H. Rao, S.M. Liao, Laminar convective heat transfer of supercritical CO_2 in horizontal miniature circular and triangular tubes, Appl. Therm. Eng. 31 (2011) 2374–2384.
[11] Y.F. Mao, L.J. Guo, B.F. Bai, X.M. Zhang, Convective heat transfer in helical coils for constant-property and variable-property flows with high Reynolds numbers, Front. Energy Power Eng. Chin. 4 (2010) 546–552.
[12] J. Taler, W. Zima, Solution of inverse heat conduction problems using control volume approach, Int. J. Heat Mass Transfer 42 (1999) 1123–1140.
[13] E.W. Lemmon, M.L. Huber, M.O. McLinden, Reference fluid thermodynamic and transport properties (REFPROP), Version8.0 In NIST Standard Reference Database 23, National Institute of Standard and Technology, Gaithersburg (MD, USA), 2007.
[14] W.R. Dean, Note on the motion of fluid in a curved pipe, Philos. Mag. 20 (1927) 208–223.
[15] H. Ito, Frictional factors for turbulent flow in curved pipes, J. Basic Eng. 81 (1959) 123–134.
[16] E.F. Schmidt, Warmeübergang und druckverlust in rohrschlangen, Chem. Eng. Technol. 13 (1967) 781–789.
[17] P.S. Srinivasan, S.S. Nandapurkar, F.A. Holland, Friction factor for coils, Trans. Inst. Chem. Eng. 48 (1970) 156–161.
[18] L.A.M. Janssen, C.J. Hoogendoorn, Laminar convective heat transfer in helical coiled tubes, Int. J. Heat Mass Transfer 21 (1978) 1197–1206.
[19] Fluent Inc., Fluent user's guide, 2006.
[20] V. Yakhot, S.A. Orszag, Renormalization group analysis of turbulence: I. Basic theory, J. Sci. Comput. 1 (1986) 1–51.
[21] L.J. Li, C.X. Lin, M.A. Ebadian, Turbulent heat transfer to near-critical water in a heated curved pipe under the conditions of mixed convection, Int. J. Heat Mass Transfer 42 (1999) 3147–3158.